Transients of the electromagnetically-induced-transparency-enhanced refractive Kerr nonlinearity

M. V. Pack, R. M. Camacho, and J. C. Howell*
Department of Physics, University of Rochester, Rochester, New York 14627, USA
(Received 13 February 2007; published 28 September 2007)

We report observations of the dynamics of electromagnetically induced transparency (EIT) in a Λ system when the ground states are Stark shifted. Interactions of this type exhibit large optical nonlinearities called Kerr nonlinearities, and have numerous applications. The EIT Kerr nonlinearity is relatively slow, which is a limiting factor that may make many potential applications impossible. Using rubidium atoms, we observe the dynamics of the EIT Kerr nonlinearity using a Mach-Zehnder interferometer to measure phase modulation of the EIT fields resulting from a pulsed signal beam Stark shifting the ground state energy levels. The rise times and transients agree well with theory.

DOI: 10.1103/PhysRevA.76.033835 PACS number(s): 42.50.Gy, 32.70.Jz

I. INTRODUCTION

Optical Kerr nonlinearities created via electromagnetically induced transparency (EIT) have received increasing attention recently because these extremely large nonlinearities have numerous applications in the fields of low-light-level and quantum optics [1–19]. Among the applications for the EIT Kerr effect are low-light-level switching [2,9,11], quantum nondemolition (QND) measurements of photon number [15], entangling optical wavepackets [7,10] and the synthesis of optical number states [5]. Also, EIT Kerr nonlinearities may play an important role in creating single-photon sources for quantum computing. For example, linear optics quantum computing requires single-photon sources and high efficiency single photon detectors [20], both of which may be enabled by EIT enhanced Kerr nonlinearities [15].

For many of the above applications the speed of the Kerr nonlinearity (i.e., the inverse of the rise time) is as important as the size of the optical nonlinearity. Pulsed applications, such as photon number resolving QND measurements, require a strong nonlinear response proportional to the pulse energy. Thus, it is the ratio between the size and the rise time of the Kerr effect that matters, not just the size. For example, although the EIT Kerr effect can be very large even at very low light level, the same parameters that make the EIT Kerr effect large also make it slow [21].

The EIT Kerr rise time is inversely proportional to the EIT linewidth, and is directly proportional to the EIT optical depth. Similarly, the size of the EIT Kerr effect is inversely proportional to the EIT linewidth, and is directly proportional to the EIT optical depth. Thus, the typical methods for increasing the size of the EIT Kerr effect leave the ratio between size and rise time unaffected.

The dependency of the EIT Kerr rise time on linewidth and optical depth have been shown theoretically, but these dependencies have not been observed experimentally. In this paper, we report experimental observations of the EIT Kerr rise time. (Note that technically there are two types of EIT Kerr nonlinearities: Refractive [2] and absorptive [3]. In this paper we discuss exclusively the refractive type of EIT Kerr nonlinearity. Observations of the dynamics of the absorptive EIT Kerr nonlinearity have been reported previously [12,22].)

Coherent transients similar to the EIT Kerr effect have been reported in a number of different contexts. Park *et al.* and Chen *et al.* have observed absorption transients in Λ-EIT media induced by rapid changes to the Raman (two-photon) detuning [23,24]. Similarly, Godone *et al.* have observed transients due to phase modulation of Raman beams in a Λ system [25]. Many others have also studied coherent transients in three level EIT systems in the contexts of coherent Raman beats [26], Zeeman splitting [27–29], and EIT in semiconductors [30,31].

In this paper we begin by reviewing the theory for EIT Kerr dynamics before presenting the experiment and measurement confirming this theory.

II. THEORY

Figure 1 shows a typical system for refractive EIT Kerr nonlinearities. Various parameters such as the Raman detuning δ_R, single-photon detuning Δ, and Rabi frequencies Ω_i where $i=\{P,C,S\}$ are defined in the figure caption. The energy levels $|1\rangle$, $|2\rangle$, and $|3\rangle$ together with the coupling field Ω_C and probe field Ω_P make up a Λ-EIT system. Coherent

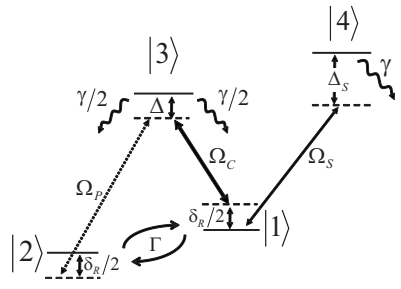

FIG. 1. Simple EIT Kerr system in a four-level *N*-type system. The detunings are defined as $\Delta_P=(\omega_3-\omega_2)-\omega_P$, $\Delta_C=(\omega_3-\omega_1)-\omega_C$, $\Delta_S=(\omega_4-\omega_2)-\omega_S$, $\Delta=(\Delta_P+\Delta_C)/2$, and $\delta_R=\Delta_C-\Delta_P$. Also, the Rabi frequencies are defined as $\Omega_i=\mu_i E_i/\hbar$ where $i=\{P,C,S\}$, μ_i is the dipole moment, and E_i is the electric field. The spontaneous emission rate out of the excited state is given by γ and Γ is the decoherence rate for the ground states.

*mvpack@pas.rochester.edu

population trapping creates a transparency resonance when the detunings of the probe and coupling fields are near Raman resonance (i.e., $\delta_R=0$). This transparency window can be very narrow with a correspondingly steep dispersion curve, and it is the steepness of the dispersion that results in large phase modulation of the probe field when the signal field perturbs the EIT system away from Raman resonance.

In Fig. 1 the signal field Stark shifts ground state $|1\rangle$ by $\Omega_S^2/4\Delta_S$, which changes the Raman detuning to

$$\delta_R(\Omega_S) = \delta_R(0) + |\Omega_S|^2/4\Delta_S. \tag{1}$$

Thus the change to the probe phase in radians is approximately

$$\Delta\phi_P \approx \frac{\omega_{32}L}{c}\frac{\partial\,\mathrm{Re}(n_P)}{\partial\delta_R}[\delta_R(\Omega_S)-\delta_R(0)] \approx \frac{L|\Omega_S|^2}{4v_g\Delta_S}, \tag{2}$$

where L is the length of the medium, $n_P \approx 1+\chi_P/2$ is the probe index of refraction, $\Omega_S=\mu_S E_S/\hbar$ is the signal Rabi frequency, μ_S is the dipole moment of the signal transition, and $v_g \approx c/[\omega_{32}\partial n_P/\partial\delta_R]$ is the group velocity for the probe [we have assumed that $|\mathrm{Re}(\chi_P)-1| \ll 1$ and $n_P \ll \omega_{32}\partial n_P/\partial\delta_R$]. This cross-phase modulation of the probe phase is a third order susceptibility $\chi^{(3)}$ because $|\Omega_S|^2 \propto E_S E_S^*$ [i.e., the medium polarization at the probe frequency is $P(\omega_P)=\chi^{(3)}E_S(\omega_S)E_S^*(-\omega_S)E_P(\omega_P)$].

The steep dispersion which makes possible ultraslow group velocities in EIT also makes the EIT Kerr nonlinearity possible. Group velocities as slow as 8 m/s [32] and 17 m/s [33] have been measured in EIT experiments and group velocities of $c\times 10^{-5}$ are routinely achieved in hot atomic vapors implying that large Kerr nonlinearities are possible at relatively low light levels. Also, the four-level EIT Kerr system does not have the large self-phase modulation Kerr nonlinearities that are present in other systems with large Kerr nonlinearities such as highly nonlinear fiber.

The theory for the dynamics of the four-level EIT Kerr system has been worked out in Ref. [21]. Because we use slightly different notation than Ref. [21] we review some of the more significant parts of the theory. First, by explicitly accounting for the energy shift of state $|1\rangle$ due to the signal [i.e., replacing $\delta_R(0)$ by $\delta_R(\Omega_S)$] we can reduce the four-level system in Fig. 1 to an approximate three-level EIT system in which level $|4\rangle$ and the signal field are not included. This approximation ignores the increases of the decoherence rate Γ due to the signal field, which is given by $\Gamma(\Omega_S)\approx\Gamma(0)+2|\Omega_S|^2\gamma_\perp/\Delta_S^2$ where $\gamma_\perp \geq \gamma/2$ is the transverse decoherence rate. Ignoring this additional decoherence is a reasonable approximation as long as $\Delta_S \gg \gamma_\perp$. In the measurement section, Sec. IV, we see that neglecting the additional decoherence creates some small discrepancies between theory and experiment, but neglecting it makes the equations much simpler.

The master equations for the reduced three-level system $|1\rangle$, $|2\rangle$, and $|3\rangle$ are

$$\dot{\rho}_{33} = -\gamma\rho_{33} + \mathrm{Im}(\Omega_2^*\rho_{32} + \Omega_1^*\rho_{31}), \tag{3}$$

$$\dot{\rho}_{22} = \frac{\gamma}{2}\rho_{33} - \Gamma\left(\rho_{22}-\frac{1}{2}\right) - \mathrm{Im}(\Omega_2^*\rho_{32}), \tag{4}$$

$$\dot{\rho}_{11} = \frac{\gamma}{2}\rho_{33} - \Gamma\left(\rho_{11}-\frac{1}{2}\right) - \mathrm{Im}(\Omega_1^*\rho_{31}), \tag{5}$$

$$\dot{\rho}_{32} = \left(i\Delta(\Omega_S) - i\frac{\delta_R(\Omega_S)}{2} - \gamma_\perp\right)\rho_{32} + i\frac{\Omega_C}{2}(\rho_{22}-\rho_{33}) + i\frac{\Omega_P}{2}\rho_{21}^*, \tag{6}$$

$$\dot{\rho}_{31} = \left(i\Delta(\Omega_S) + i\frac{\delta_R(\Omega_S)}{2} - \gamma_\perp\right)\rho_{31} + i\frac{\Omega_P}{2}(\rho_{11}-\rho_{33}) + i\frac{\Omega_C}{2}\rho_{21}, \tag{7}$$

and

$$\dot{\rho}_{21} = [i\delta_R(\Omega_S) - \Gamma_\perp]\rho_{21} - i\frac{\Omega_P}{2}\rho_{32}^* + i\frac{\Omega_C^*}{2}\rho_{31}, \tag{8}$$

where $\gamma_\perp=(\gamma+\Gamma)/2+\gamma'$ is the transverse decoherence rate for the excited state coherences and $\Gamma_\perp=(\Gamma'+\Gamma)$ is the ground state coherence decay rate. The primed decoherence rates γ' and Γ' are dephasing rates (i.e., loss of coherence without transfer of population from one state to another).

When the excited state coherences ρ_{13} and ρ_{23} can be adiabatically eliminated (this assumption is easily satisfied for our choice of experimental parameters), the three-level master equation simplifies to a two-level Bloch vector equation [34]. Additionally, the adiabatic elimination of the excited state coherences makes it possible to write the probe susceptibility as a simple function of the coherence between the ground states ρ_{21}:

$$\chi_P(\rho_{21}) \approx \frac{N\rho_{22}|\mu_{32}|^2}{2\epsilon_0\hbar}\frac{1-(\rho_{21}/\rho_{21}^{(-)})^*}{\Delta-\delta_2+i\gamma_\perp}, \tag{9}$$

where N is the atomic density, $\rho_{21}^{(-)}=-\Omega_P^*\Omega_C/\Omega^2 \approx -\Omega_P^*/\Omega$ is the ground state coherence (GSC) of the dark state, and $|-\rangle=\Omega_P|1\rangle-\Omega_C|2\rangle$ is the dark state. This result also assumes that $\rho_{22}\approx\Omega_C^2/\Omega^2$, $\rho_{11}\approx\Omega_P^2/\Omega^2$, and both fields are below saturation $\Omega_C \ll \gamma$ [21]. Finally, the equations simplify even more when we assume the fields are real and positive, the single-photon detuning is zero, $\Delta=0$, and the Raman detuning is much smaller than the homogeneous linewidth $\delta_R \ll \gamma_\perp$. All of the above assumptions are valid for the experimental parameters discussed in this paper.

Expressing the susceptibility as a function of the GSC, as is done in Eq. (11), has several advantages for discussing the dynamics of the EIT Kerr nonlinearity. The primary advantage is that the dynamics and rise times of the GSC have a physically intuitive interpretation. Also, the GSC interpretation results in simple analytic expressions for the steady-state and transient solutions of the Bloch vector equation.

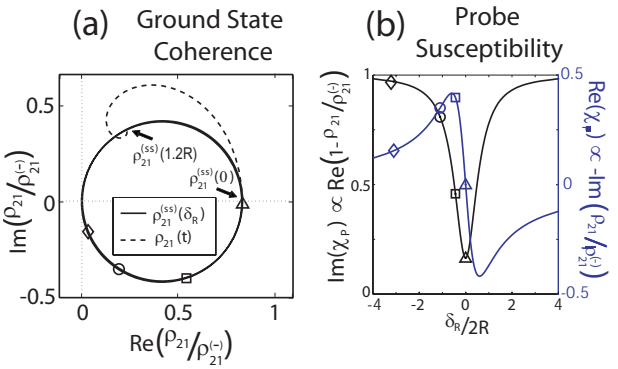

FIG. 2. (Color online) (a) Steady-state (solid line) and transient (dashed line) ground state coherences are plotted in the complex plane, while (b) the probe susceptibility is plotted as a function of the Raman detuning δ_R. All plots are theoretical with $R \approx 5\Gamma$, and all variables except the Raman detuning are held constant. The transient ground state coherence curve (dashed) started with steady state for $\delta_R=0$, then suddenly the Raman detuning changed to $2R$. To show the mapping between ground state coherence and probe susceptibility four shapes corresponding to four Raman detunings have been plotted on both the steady-state ground state coherence and susceptibility curves.

Both of these advantages are demonstrated in Fig. 2. First, Fig. 2(a) shows that the steady-state GSC as a function of Raman detuning is a circle (solid line) in the complex plane; mathematically this is

$$\rho_{21}^{(ss)}(\delta_R) = \frac{\rho_{21}^{(-)} R}{(R+\Gamma) - i\delta_R}. \tag{10}$$

The optical pumping rate $R \approx \Omega^2/\gamma_\perp$ is the rate at which optical pumping transfers atoms from the bright state to the dark state. Figure 2(b) shows the real (black line) and imaginary (gray line) parts of the steady-state probe susceptibility,

$$\chi_p^{(ss)} \approx -i\frac{\alpha_p c}{\omega_{32}} \frac{\delta_R^2 + \Gamma[(R+\Gamma) + iR\delta_R]}{(R+\Gamma)^2 + \delta_R^2}, \tag{11}$$

plotted as a function of the Raman detuning, where $\alpha_p = N\rho_{22}|\mu_{32}|^2/2\hbar\epsilon_0\gamma_\perp$ is the probe absorption coefficient. To help visualize the mapping of Eq. (11) between GSC and probe susceptibility, corresponding points on the GSC and susceptibility plots in Fig. 2 are indicated by various shapes (e.g., triangle, square, circle, diamond).

The dashed line in Fig. 2(a) shows a trajectory of the dynamical evolution of the GSC. Mathematically these trajectories are given by

$$\rho_{21}(t) = \rho_{21}^{(ss)} + [\rho_{21}(0) - \rho_{21}^{(ss)}]e^{t(i\delta_R - R - \Gamma)} \quad \text{for } t \geq 0, \tag{12}$$

where $\rho_{21}(0)$ is the initial GSC and all parameters are held constant for times $t>0$ with a steady-state GSC of $\rho_{21}^{(ss)}$. When the final conditions have $\delta_R \geq R$ the trajectories follow spiral patterns similar to the trajectory shown in the dashed line in Fig. 2(a), and when the final Raman detuning is $|\delta_R| \ll R$ the trajectories are essentially straight lines from $\rho_{21}(0)$ to $\rho_{21}^{(ss)}$.

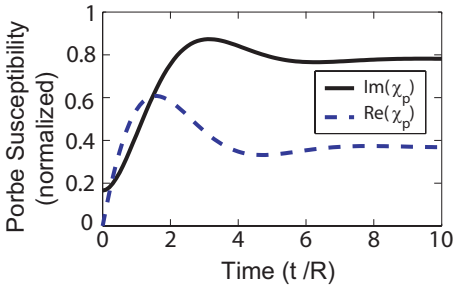

FIG. 3. (Color online) The real and imaginary parts of the probe susceptibility plotted as a function of time. The same parameters have been used as in Fig. 2 (i.e., $R \approx 5\Gamma$, for $t \leq 0$, $\delta_R=0$, and for $t>0$, $\delta_R=2R$).

Figure 3 shows the EIT Kerr transients in the time domain [this is the same trajectory as the dashed line in Fig. 2(a)]. Plotted as a function of time the real and imaginary parts of the susceptibility exhibit damped simple harmonic oscillations.

From transient curves, like those in Fig. 3, it is possible to find the $1/e$ rise times for the refractive and absorptive parts of the EIT Kerr nonlinearity. Figure 4 shows these rise times as a function of Raman detuning. The refractive and absorptive rise times approach two different sets of asymptotes in the large Raman detuning limit $\delta_R \gg R$ and in the small Raman detuning limit $\delta_R \ll R$ (the condition for EIT is $R \gg \Gamma$ making $R+\Gamma \approx R$).

For most refractive EIT Kerr applications it is generally desirable to work near Raman resonance with changes in Raman detuning that are small relative to the EIT linewidth. That is, $\delta_R \ll R$ for all times. This provides a maximal refractive Kerr nonlinearity with minimal change in absorption. In this small Raman detuning regime, $\delta_R \ll R$, the $1/e$ rise and fall times for refraction are given by

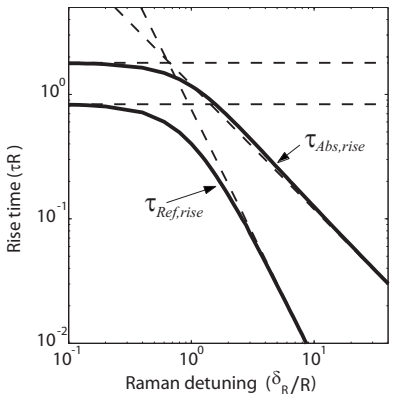

FIG. 4. Solid lines show the $1/e$ rise time for absorption and refraction resulting from the EIT Kerr nonlinearity. Rise times are plotted logarithmically as a function of the magnitude of the Raman detuning δ_R. All quantities are dimensionless and normalized by the optical pumping rate R, and $\Gamma/R=0.2$. For small detunings the rise times asymptotically approach $\tau_{abs}=2.15/(R+\Gamma)$ and $\tau_{ref}=1/(R+\Gamma)$. For large two-photon detunings the rise times asymptotically approach $\tau_{abs}=1.2/\delta_R$ and $\tau_{ref}=0.63(R+\Gamma)/\delta_R^2$. These asymptotes are shown as the dashed lines.

$$\lim_{\delta_R \to 0} \tau_{\text{ref,rise}} = \lim_{\delta_R \to 0} \tau_{\text{ref,fall}} = \frac{1 + \tilde{\alpha}_p z/4}{R + \Gamma} \tag{13}$$

and the absorption rise and fall times are

$$\lim_{\delta_R \to 0} \tau_{\text{abs,rise}} = \frac{1 + (1 + \tilde{\alpha}_p z/2)c_1}{R + \Gamma} \tag{14}$$

and

$$\lim_{\delta_R \to 0} \tau_{\text{abs,fall}} = \frac{1 + 3c_1 \tilde{\alpha}_p z/8}{R + \Gamma}, \tag{15}$$

where $c_1 = \ln\{2 + \ln[2 + \ln(2 + \cdots)]\}$, and $\tilde{\alpha}_p = \alpha_p R/(R+\Gamma)$ is the depth of the EIT; the atoms occupy the half space $z \geq 0$. The probe and coupling fields are copropagating from smaller z to larger z. These rise/fall times can be calculated analytically for small optical depths $\tilde{\alpha}_p z \ll 1$. For large optical depths the dependence of these rise and fall times on $\tilde{\alpha}_p z$ was determined by curve fitting numerical simulations of an optically thick four-level system.

These rise and fall times can be understood intuitively as the ratio between the total phase change of the GSC $\Delta\theta$ and the rate of GSC phase change $\dot{\theta}$ (we use θ for the phase of the GSC, and ϕ for the phase of the probe field). In the limit $\delta_R \ll R$ and $\Omega_C \gg \Omega_P$ the optically thick equivalent of Eq. (10) is

$$\rho_{21}^{(ss)}(z) \approx \frac{\Omega_P(z)}{\Omega_P(0)} \frac{\rho_{21}^{(-)} R}{R + \Gamma} \exp\left(i \frac{\delta_R}{R + \Gamma}\right), \tag{16}$$

where

$$\Omega_P(z) \approx \Omega_P(0) \exp\left[-\frac{z\alpha_p}{2(R+\Gamma)}\left(\Gamma + i\frac{R\delta_R}{R+\Gamma}\right)\right], \tag{17}$$

and we have assumed $\Omega_C(z) \approx \Omega_C(0)$. The total GSC phase change is $\Delta\theta = \delta_R(1 + z\alpha_p/2)/(R+\Gamma)$, and from Eq. (12) we see that $\dot{\theta} = \delta_R$. Thus, we expect the rise time to be approximately

$$\tau \sim \Delta\theta/\dot{\theta} = (1 + z\tilde{\alpha}_p/2)/(R + \Gamma).$$

In the large Raman detuning limit, i.e., $\delta_R \gg (R+\Gamma)$, the rise times become more complicated. However, for small optical depths the large-Raman-detuning rise times are still straightforward to calculate. In this regime the GSC phase change is $\Delta\theta \approx \pi - \delta_R/(R+\Gamma)$, and the rise times are

$$\lim_{\delta_R \to \infty} \tau_{\text{abs,rise}} = \frac{\arccos[e^{-1} + (R+\Gamma)/\delta_R]}{\delta_R} \tag{18}$$

and

$$\lim_{\delta_R \to \infty} \tau_{\text{ref,rise}} = \frac{(1 - e^{-1})(R+\Gamma)}{\delta_R^2}. \tag{19}$$

For negligible optical thickness (i.e., $\alpha L \gg 1$), the asymptotic rise times from Eqs. (13), (14), (18), and (19) are shown in Fig. 4 as dashed lines to compare with the exact rise times.

This simple four-level model provides a simple intuitive picture for how the EIT Kerr nonlinearity evolves as a function of time, and almost all of the ideas presented in this section generalize to the more complicated experimental system discussed in the next sections. However, there are differences between the simplified theory and the experimental reality, and we discuss these differences as they become important.

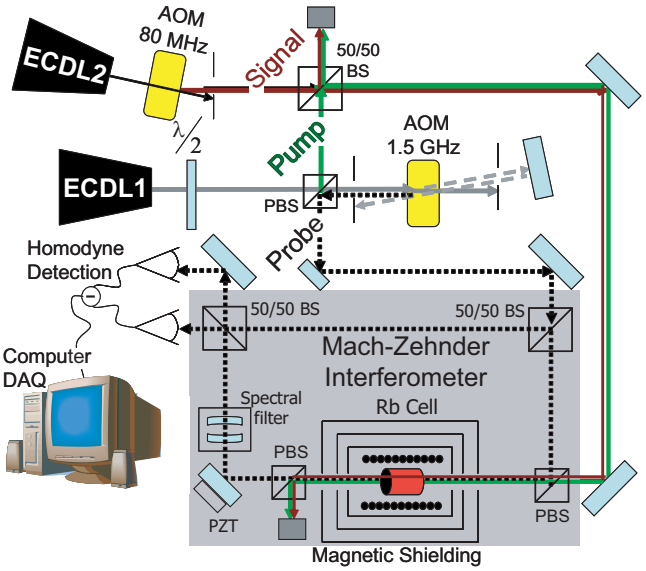

FIG. 5. (Color online) Schematic of the experimental apparatus. The probe beam is sent through a Mach-Zehnder interferometer to measure changes in the relative phase between the two arms of the interferometer. The coupling and signal beams interact with the probe in the rubidium cell before being separated from the probe via polarization and spectral filtering. A computer controlled data acquisition system records and averages the difference signal from balanced homodyne detection.

For applications of the refractive EIT Kerr nonlinearity, Eq. (13) is the most significant result of this section. This equation shows that when $\delta_R \ll R$ the rise times are dependent on only two parameters: The optical depth $\alpha_p L$ and the EIT linewidth FWHM $= 2(R+\Gamma)$, both of which are straightforward to measure experimentally. For large Raman detunings $\delta_R \gg R$, the rise times are also dependent on the size of the Stark shift (i.e., Raman detuning) which is also an experimentally tunable parameter.

III. EXPERIMENT

Using a Mach-Zehnder interferometer as shown in Fig. 5, we observed the transients of EIT on the D_1 line of ^{85}Rb. The transients are created by pulsing the signal beam which is about 2 GHz red detuned from the ^{85}Rb D_2 $F=2 \rightarrow F' = \{2,3\}$ transitions. Previous experiments used frequency modulation spectroscopy to observe similar Stark shifts and refractive EIT Kerr nonlinearities [11], but such experiments are unable to observe the transient behavior of the systems because they require lock-in amplification. Thus this is a direct observation of the dynamics and rise times of the refractive EIT Kerr nonlinearity.

Both probe and coupling fields are obtained from a single external cavity diode laser (ECDL1 with wavelength λ

=795 nm) by splitting the beam at a polarizing beam splitter (PBS) to obtain a coupling beam and a probe beam. The probe beam is double passed through a 1.5 GHz acousto-optic modulator (AOM) to shift its frequency by approximately 3 GHz the ground state hyperfine splitting of ^{85}Rb. Deriving both EIT fields from a single laser ensures the excellent phase coherence necessary for good EIT. Additionally, we are able to control the frequency difference between probe and coupling precisely via the microwave frequency synthesizer driving the AOM.

A second laser (ECDL2 with wavelength $\lambda=780$ nm) is pulsed using an 80 MHz AOM with 50 ns rise time to create the signal pulses. Both ECDL lasers are New Focus Vortex lasers (i.e., they are single-mode external-cavity-feedback diode lasers with linewidths of less than 300 kHz). The signal and coupling beams are combined on a 50/50 beam splitter (BS) and are both horizontally polarized so they can be coupled into the Mach-Zehnder interferometer via a PBS.

The probe is split into two paths in the Mach-Zehnder interferometer: a reference local oscillator path and a probe path that goes through the cell (the reference field is about a factor of two larger than the probe field $E_R \sim 2E_p$). After the Mach-Zehnder interferometer, balanced homodyne detection measures changes in the probe phase. Changes in probe amplitude can also be measured by blocking the reference arm of the interferometer and measuring the current from just one of the photodiodes. Both polarization and spectral filtering are used after the cell to isolate the probe field from the coupling and signal fields. When necessary the relative phase of the two arms of the interferometer scanned and locked using the piezomounted mirror (PZT) after the cell. The homodyne signal is given by

$$Q \propto |E_R||E_P|\sin[\phi_{pv} + \mathrm{Im}(\chi_p)k_P L], \tag{20}$$

where E_R is the electric field amplitude in the reference leg of the interferometer, ϕ_{pv} is the relative phase between the two arms of the interferometer controlled via the piezovoltage, L is the length of the cell, and $k_P=\omega_P/c$ is the wave number of the probe field.

The cell apparatus consists of three layers of magnetic shielding with a long solenoid inside the innermost layer of magnetic shielding. In addition to containing 20 torr of nitrogen buffer gas, the rubidium cell contains both rubidium isotopes in their natural abundance (27.8% ^{87}Rb and 72.2% ^{85}Rb). The cell is cylindrical in shape with a length of 30 mm and a diameter of 25.4 mm. The number density of rubidium atoms is controlled by heating the cell with electrical strip heaters positioned between the outer and middle layers of magnetic shielding.

At the output of the Mach-Zehnder interferometer the homodyne signal is measured using two reverse biased Hamamatsu S2830 photodiodes soldered for differential detection. After the photodiodes a 1 MHz low-noise transimpedance amplifier prepares the signal for computer controlled data acquisition (DAQ). CW measurements are recorded by the DAQ, and the fast transient data are recorded and averaged using a 1.5 GHz bandwidth oscilloscope.

Figure 6 shows the hyperfine levels for the ^{85}Rb D_1 and D_2 lines with laser transitions that are driven in the experiment. The hyperfine splittings for the $5P_{1/2}$ (361 MHz) and $5P_{3/2}$ (<220 MHz) hyperfine levels are much smaller than the Doppler width (600 MHz), such that the individual hyperfine levels cannot be resolved. Additionally, rubidium-nitrogen collisions create a rapid interchange of atoms among the velocity classes without decohering the GSC, which means that all EIT parameters such as optical pumping R and linewidths γ must be averaged over all velocity classes (see the Appendix). Finally, the signal field Stark shifts both ground hyperfine levels resulting in a total change in Raman detuning of

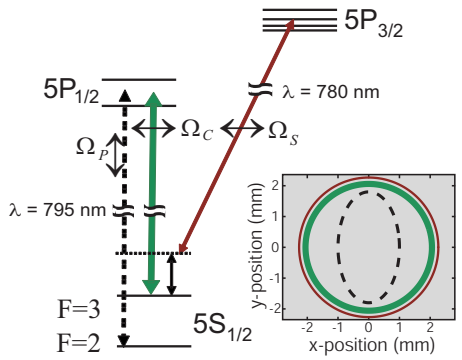

FIG. 6. (Color online) Level diagram of ^{85}Rb D_1 and D_2 lines with the primary transitions excited by the probe, coupling, and signal fields. The inset shows the approximate beam sizes and shapes for the probe ($w_{p,x}=1$ mm and $w_{p,y}=1.8$ mm), coupling ($w_c=2.1$ mm), and signal ($w_s=2.2$ mm) fields.

$$\delta_R(\Omega_S) = \delta_R(0) + \frac{\Omega^2 \Delta_{\mathrm{hf}}}{4\Delta_S(\Delta_S + \Delta_{\mathrm{hf}})}, \tag{21}$$

where $\Delta_{\mathrm{hf}}=2\pi\times 3.0357$ GHz is the hyperfine splitting of the ground states.

The inset in Fig. 6 shows the approximate $1/e^2$ intensity beam shapes for the coupling, probe, and signal fields (in the experiment the beams were not perfectly centered). The coupling and signal beams were essentially identical with beam radius of $w_c \approx w_s=2.2$ mm, while the probe beam was smaller and slightly elliptical $w_{p,x}=1.0$ mm and $w_{p,y}=1.8$ mm.

IV. MEASUREMENTS

To verify the dependence of the EIT Kerr dynamics on optical depth, EIT linewidth, and Raman detuning, we measured the transient and CW response of EIT to the signal field while varying the cell temperature (optical thickness αL), coupling intensity [EIT linewidth $(R+\Gamma)$], and signal intensity (Stark shift δ_R). The different conditions under which data were taken are summarized in Table I. Each row in Table I corresponds to a different set of data in which both CW and transient measurements were taken for several signal powers ranging from 0.2 mW to 4.9 mW. In all measurements the probe power was 40 μW, and the signal detuning was $\Delta_S=2\pi\times 1.9$ GHz. In the following sections we primarily present the data for the first row of Table I, but the same analysis was carried out for each row of Table I.

TABLE I. Several measured parameters for the EIT line shapes with no signal present. The beam powers were measured immediately before the PBS in front of the vapor cell. αL is the maximum absorption experienced far from Raman resonance. $\tilde{\alpha}L$ is the difference between maximum absorption and the absorption minimum near Raman resonance, and EIT FWHM is self-explanatory.

Temperature	Power coupl.	αL total	$\tilde{\alpha}L$ EIT depth	EIT (FWHM)
58 °C	340(20) μW	5.2(3)	3.7(1)	11.5(7) kHz
58 °C	1.0(1) μW	5.3(2)	4.3(1)	31.9(1.2) kHz
58 °C	1.9(1) μW	5.5(2)	4.6(1)	58.1(1.8) kHz
48 °C	1.0(1) μW	2.0(1)	1.5(1)	31.9(7) kHz
52 °C	1.0(1) μW	3.3(1)	2.6(1)	33.2(7) kHz
72 °C	1.0(1) μW	20.4(9)	16.4(7)	41(3) kHz

A. CW measurements

Figure 7 shows the CW probe absorption as a function of Raman detuning for several different signal powers, with a cell temperature of 58 °C and a coupling power of 0.34 mW (first row in Table I). Figures 10–15 also use this same data set. In addition to the signal field Stark shifting the absorption minimum, the signal field also causes the transparency resonance to become shallower and broader. These effects are largely due to the additional decoherence created by the signal field [i.e., $\Gamma(\Omega_S)=\Gamma(0)+\Omega_S^2\gamma_\perp/\Delta_S^2$], which is not explicitly included in the theory of Sec. II. This additional decoherence is most noticeable when the optical pumping is of the same order of magnitude as the decoherence rate (i.e., $R\sim\Gamma$), which is the case for the data corresponding to row 1 of Table I. For all other sets of parameters in Table I the optical pumping R is a factor of 3–6 times larger than for row 1 and the broadening is significantly less noticeable.

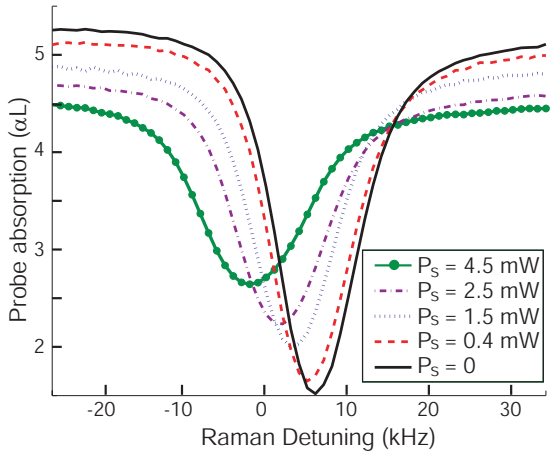

FIG. 7. (Color online) Probe absorption versus Raman detuning for different CW signal powers. The signal detuning is $\Delta_S=2\pi\times1.9$ GHz and the coupling (probe) power is 340 μW (40 μW). The fact that with no signal field Raman resonance is already shifted away from the expected zero is due mostly to the 20 torr N_2 buffer gas shifting the hyperfine splitting ($\Delta\omega_{hf}=2\pi\times240$ Hz per torr N_2). The probe and coupling also cause a small (about 1 kHz) Stark shift at these powers.

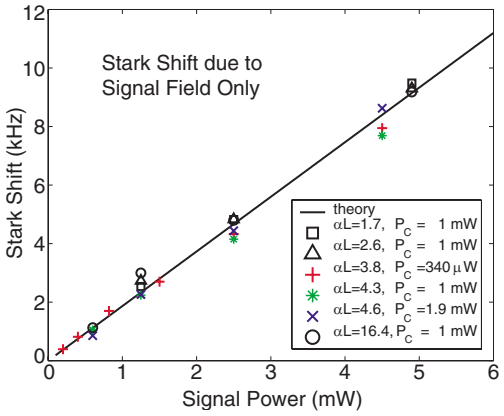

FIG. 8. (Color online) Stark shift due to the signal field for several settings of coupling power and EIT optical depth.

From the displacement of the probe absorption minimum we determined the Stark shift as a function of signal power (shown in Fig. 8). Figure 8 shows the Stark shifts due to the signal field only for all rows of Table I.

There is also a Stark shift due to the coupling field interacting with the probe transitions and a Stark shift due to the probe field interacting with the coupling transitions. This Stark shift is plotted as a function of coupling power in Fig. 9. Also, plotted in Fig. 9 is the transparency linewidth versus coupling power. The linewidth and Stark shift are also slightly dependent on the probe power, but probe power is sufficiently small that it can be neglected. Figures 8 and 9 exhibit the expected linear dependence on intensity.

In addition to measuring the imaginary part of the probe susceptibility via the probe absorption, we also measured the refractive part of the susceptibility using balanced homodyne detection shown in Figs. 10 and 11. The homodyne signal was measured by setting the phase ϕ_{pv} to a desired value and then stepping the Raman detuning over the desired range with a dwell time of 200 ms or greater at each Raman detuning.

Figure 10 shows the homodyne signal for the first row of Table I with no signal field (black) and a signal power of

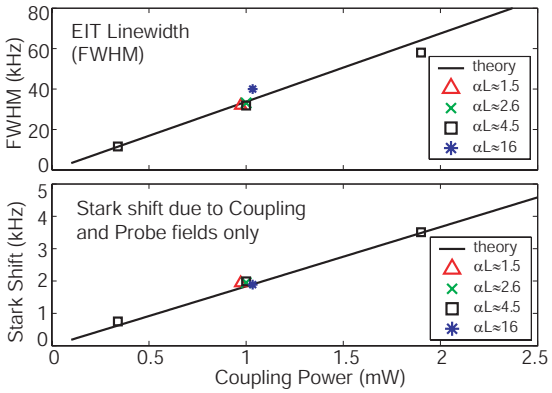

FIG. 9. (Color online) Stark shift due to the coupling and probe fields as a function of coupling power. Also shown is the FWHM of the EIT resonance versus coupling power. The signal was off for all of these measurements.

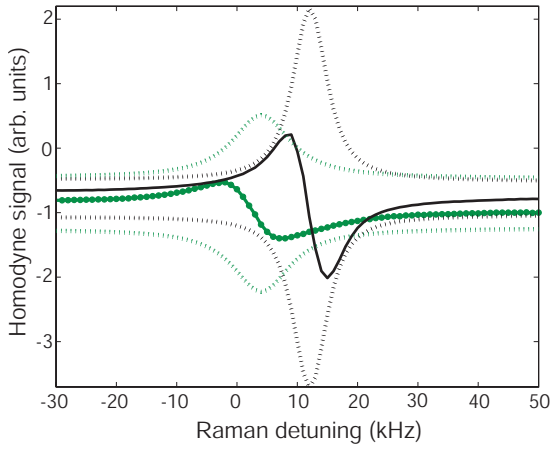

FIG. 10. (Color online) Raw CW homodyne data for coupling power of 340 μW. Two sets of data are shown: one for P_s=0 and the other for P_s=4.5 mW. The dotted lines show the homodyne envelope (i.e., the maximum and minimum values which the homodyne signal can obtain).

4.5 mW (nonblack). The dashed curves show an envelope of maximum and minimum homodyne signal [i.e., $\pm|E_r||E_p(\delta_R)|$], which is determined for each Raman detuning δ_R by measuring amplitude of the homodyne sinusoid when the phase ϕ_{pv} is scanned over several cycles. In Fig. 11 we have used the data from Fig. 10 to calculate the real and imaginary parts of the probe susceptibility. The homodyne envelope gives the absorptive (imaginary) part of the probe susceptibility, and the refractive (real) part of the probe susceptibility is extracted using Eq. (20), the homodyne envelope, and the homodyne signal.

B. Transients measurements

Homodyne detection was also used to measure the transient response of the probe field when the signal field is turned on and off with a fast rise time. Figure 12 shows the transient homodyne signal and homodyne envelope when the

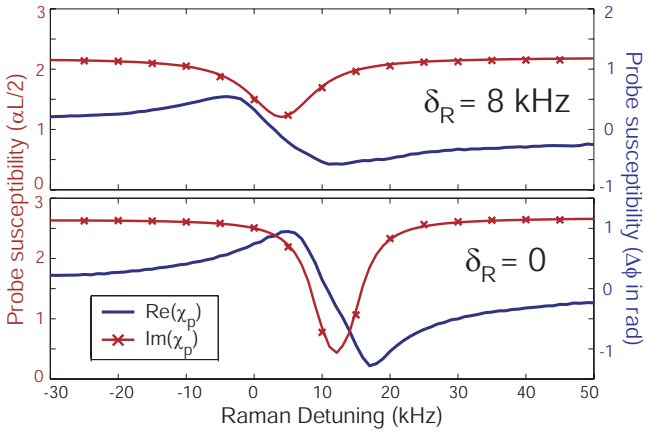

FIG. 11. (Color online) Measured absorption αL and phase shift $\Delta\phi$ derived from the homodyne data in Fig. 10. In addition to obtaining refraction information we are able to confirm the absorption measurements shown in Fig. 7.

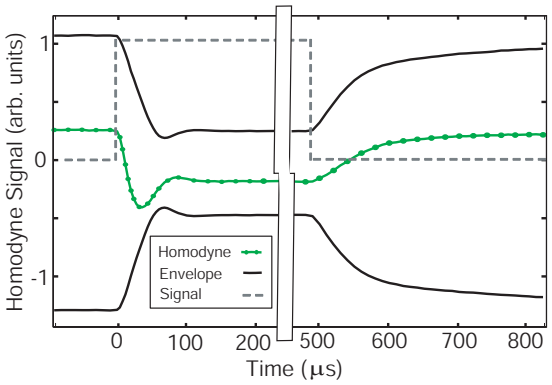

FIG. 12. (Color online) Homodyne measurements as a function of time (P_s=4.5 mW, P_c=340 μW). The signal was turned on at t=0 and then turned off again at t=500 μs. Similar to Fig. 10, the envelope shows the maximum and minimum values obtainable by the homodyne signal.

peak signal power was 4.5 mW and all other parameters are given by the first row in Table I. From these measurements, the absorptive and refractive transients of the probe field can be extracted. Figure 13 shows the extracted change in probe absorption and probe phase for different choices of peak signal power. The inset shows the measured absorption and dispersion curves from Fig. 11 when P_S=0. The vertical lines in the Fig. 11 inset show the Stark shifts corresponding to different signal powers. The square dashed line in Fig. 11 shows the time during which the signal was on.

There are several characteristics of these transients worth noting. First, the steady-state changes in absorption and refraction can be estimated by looking at the Fig. 11 inset. The real and imaginary parts of the susceptibility are Stark shifted from their Raman resonance values to approximately those values indicated by the vertical lines in the Fig. 11 inset. For example, for small signal powers (e.g., P_S =0.2 mW and P_S=0.4 mW) the change in refraction is larger than the change in absorption, because near Raman reso-

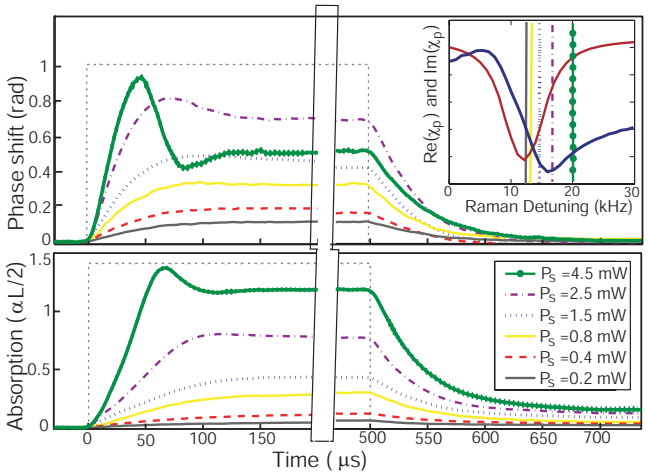

FIG. 13. (Color online) Change in refraction and absorption as a function of time for different values of peak signal power. Both refraction and absorption are measured relative to their respective values when the signal is off.

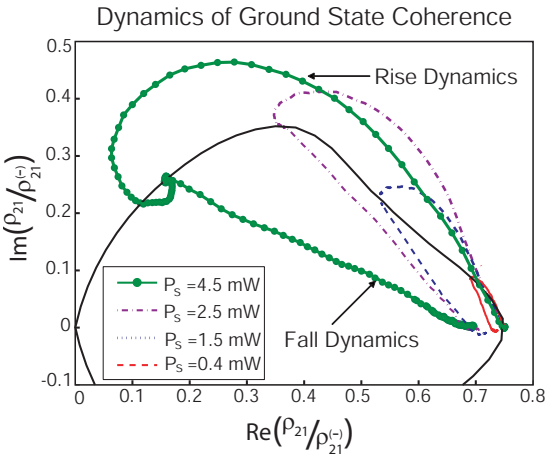

FIG. 14. (Color online) Trajectories of the ground state coherence GSC in the complex plane. GSC was derived using Eq. (11) and the refraction and absorption transients in Fig. 13. Steady state GSC values (black line) and transient data (nonblack textured lines) are both shown. The curved or spiraling lines show the rise dynamics ($\delta_R \neq 0$), while the straighter lines show the fall dynamics ($\delta_R = 0$).

nance the slope of the dispersion curve is greater than the slope of the absorption curve. According to the theory from Sec. II the change in absorption is quadratic for small Stark shifts around Raman resonance. However, the theory neglects the small linear change in the absorption due to the increase in decoherence $\Gamma(\Omega_S)=\Gamma(0)+2\Omega_S^2\gamma_\perp/\Delta_S^2$ arising from the signal field. For small signal powers the Stark shift is a constant.

For large signal fields the rise time decreases and the oscillatory nature of the transients becomes more noticeable. The fall time is independent of the signal field and is never oscillatory because $\delta_R \approx 0$ when the signal field is off.

Additional insight comes from considering the dynamics of the GSC. In Fig. 14 we have used the inverse mapping of Eq. (11) to obtain the measured GSC transients. The real part of the GSC is plotted versus the imaginary part of the GSC parametrically as a function of time. The rise dynamics look very similar to the transient trajectory shown in the theory plot in Fig. 2. The fall dynamics are essentially straight lines back toward the dark state GSC.

Figure 15 shows measured $1/e$ rise and fall times for the transient measurements presented in Fig. 13. The solid lines are theoretical rise times in which optical thickness is accounted for by multiplying the theory curves from Fig. 4 by the factor $(1+\tilde{\alpha}L/4)$ for the refractive curves and the absorptive theory curves have been multiplied by $1+c_1\tilde{\alpha}L/(2+2c_1)$. The fall times are mostly independent of the size of the Stark shift as expected (the theory curves are only for the rise times, not the fall times). The theory curves agree very well with the measured rise times, except for the absorptive rise and fall times for small Stark shifts. For small Stark shifts the change in absorption is very small, as can be seen in Fig. 13, making this discrepancy of little practical importance. Also, there is no simple analytic theory for the rise time when the Stark shift is large (i.e., $\delta_R \sim R$), so it is somewhat surprising that the theory curves agree as well as they do in this region.

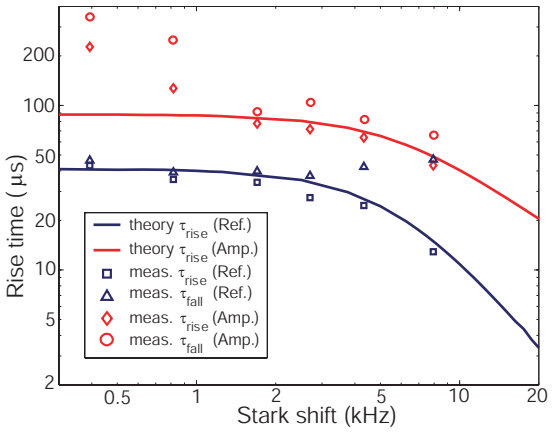

FIG. 15. (Color online) Rise times of the refraction and absorption resulting from the EIT Kerr nonlinearity ($P_c=340$). Squares and triangles show the measured refractive rise and fall times. Diamonds and circles show the measured absorptive rise and fall times, and solid curves are theory for the rise times. The values $\tilde{\alpha}L=3.75$ and $R+\Gamma=2\pi$ kHz are used to obtain the theory curve fit.

Figure 16 shows the rise time plots for the data sets corresponding to the second through fifth rows of Table I. For each data set in Fig. 15 we include the EIT half width at half maximum, HWHM$=R+\Gamma$, and EIT depth which were used to calculate the theory curves.

Finally, Fig. 17 shows the measured and theoretical rise times versus optical thickness for small Stark shifts. The measured refractive rise and fall times fit the theory curve well. For small optical depths $\alpha L<6$ the absorptive rise time agrees with theory. However, the absorptive fall times differ from the theory, and both absorptive rise and fall times disagree with theory for large optical depths. It is not clear why these differences exist, and they are not significant for appli-

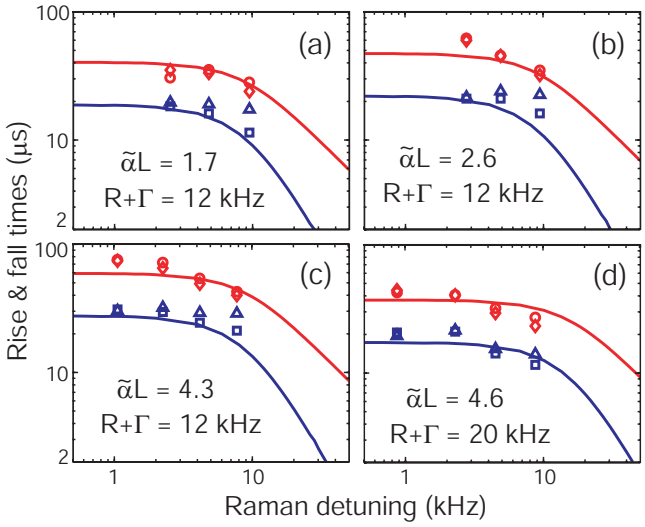

FIG. 16. (Color online) Rise- and fall-time measurements for the conditions (a) $T=48$ °C and $P_c=1$ mW, (b) $T=52$ °C and $P_c=1$ mW, (c) $T=58$ °C and $P_c=1$ mW, and (d) $T=58$ °C and $P_c=1.9$ mW. The definitions for measured data and curve fits are the same as in Fig. 15, and the parameters used in the curve fits are given in each figure.

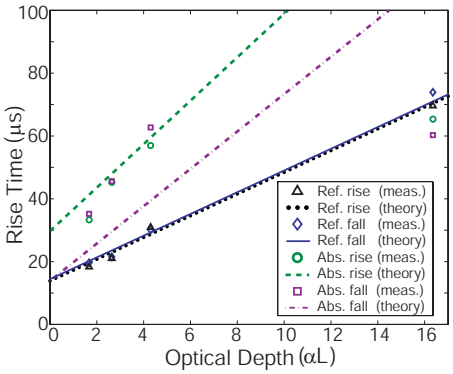

FIG. 17. (Color online) Rise and fall times for the refractive and absorptive parts of the EIT Kerr nonlinearity versus optical depth. The Stark shift is small $[\delta_R \ll (R+\Gamma)]$ for all measurements and theory.

cations based on the refractive EIT Kerr nonlinearity.

V. DISCUSSION

Although the simple theory from Sec. II shows general agreement with the measured results, there are several differences which should be explained. These differences mostly arise from two sources: Approximations made in the theory, and the experimental system is more complicated than the theoretical system (note that the theoretical system assumes plane waves, a single velocity class, and a four-level atom).

We have already mentioned that in addition to creating the Stark shift the signal field also adds to the decoherence between ground states; i.e.,

$$\Gamma(\Omega_S) \approx \Gamma(0) + \Omega_S^2 \gamma_\perp / \Delta_S^2. \tag{22}$$

By leaving this additional decoherence out of the theory (see Sec. II) the equations become simpler, but this also leads to some inaccuracy. Figure 18 illustrates the results of neglecting the signal dependent decoherence, by comparing the measured and theoretical GSC dynamics. First, the measured steady-state GSC is not a circle as predicted by the theory. In the theory near $\delta_R=0$ the change in refraction is linear in signal intensity $[\mathrm{Re}(\Delta\chi_p) \propto \mathrm{Im}(\rho_{21}) \propto \Omega_S^2]$ whereas the absorption is quadratic in signal intensity $[\mathrm{Im}(\Delta\chi_p) \propto \mathrm{Re}(\rho_{21}) \propto \Omega_S^4]$ resulting in a smooth quadratic steady-state GSC curve near Raman resonance. However, in reality both the absorption and refraction have a linear dependence on the signal, and the measured steady-state GSC curve comes to a cusp near Raman resonance. The signal dependent decoherence is also the source for the differences between the transient measured and theoretical GSC curves. When the signal dependent decoherence is used in calculations simple analytic results are no longer possible but the theory agrees much more closely with measurements. Even with its inadequacies the theory does a good job of predicting the measurements as shown in Fig. 18.

Other differences arise because the experimental system is actually a collection of many systems (i.e., velocity classes, etc.) that must be averaged. This averaging takes several forms. First, the ^{85}Rb level structure for the D_1 and D_2 lines is rather complicated (eight hyperfine levels and 48 magnetic sublevels) resulting in five dark states and seven bright states. Second, at room temperature ^{85}Rb experiences significant Doppler broadening, requiring us to average over atoms from different velocity classes. Finally, the experiment uses Gaussian-like beams with spatially varying intensities, requiring spatial averaging.

The experimental EIT Kerr system with a total of 48 levels will obviously be more complicated than the four-level system assumed in Sec. II. Even so, the theory of Sec. II accurately predicts most experimental observations. One significant difference resulting from the experimental level structures is that four of the five dark states are only semidark. These semidark states are much darker than bright states, but they are still weakly coupled with the excited states resulting in nonzero transparency even when $\Gamma=0$. For the parameters in the experiment these semidark states limit our best transparency to about $\alpha L/7$. The Appendix has the details about how we average over dark states and velocity classes to obtain the effective optical pumping rate R_{ave} and homogeneous linewidth γ_{eff}.

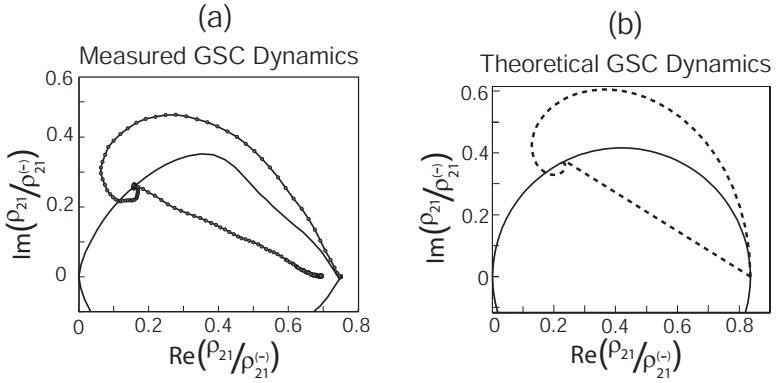

FIG. 18. (a) Measured transient (solid line with dots) and steady-state (solid line) GSC and (b) transient (dashed line) and steady-state (solid line) GSC calculated using the theory from Sec. II. Both plots show the normalized real part of the GSC plotted versus the imaginary part of the GSC. The GSCs are plotted parametrically as a function of time (transient data), or as a function of Raman detuning (steady-state data). The transient data show GSC starting out in steady state for zero Raman detuning, and evolving toward steady state when the Raman detuning is $\delta_R \approx 1.2(R+\Gamma)$, after which the Raman detuning is sharply switched back to zero, and the GSC again evolves toward steady state.

The spatial averaging over variations in field intensities has the primary result that the simple relation between the rise times and the EIT HWHM must be slightly modified to become

$$\tau_{\mathrm{ref}} = f\frac{1+\tilde{\alpha}L/4}{(\mathrm{HWHM})}, \tag{23}$$

where HWHM$=R+\Gamma$ and f is a integration factor accounting for spatial averaging. The factor f arises because the effect of spatial averaging is slightly different for the $1/e$ rise time and the HWHM. Diffusion is also important in spatial averaging because it tends to coarse-grain the averaging. The characteristic diffusion length is $l_D \equiv \sqrt{\bar{v} l_0 T_R}$, where $\bar{v}$ is the mean velocity, l_0 is the mean free path length between ^{87}Rb-N_2 collisions, and $T_R \equiv 1/R$ is the optical pumping period. Atoms that are within the characteristic diffusion length will on average have encountered the same average field intensity over the last optical pumping period T_R regardless of the difference between the field intensities at their current locations. This diffusion length sets the characteristic length for coarse graining the spatial average.

In the experiment transit-time broadening [35] is the dominant source of GSC decoherence, which means that the diffusion length is related to the beam waist by $R/\Gamma \sim (w_p/l_D)^2$ (the probe beam waist w_p is the limiting beam waist). Thus, when $R \sim \Gamma$ the diffusion length is similar to the beam diameter and $f \approx 1$ and spatial averaging does nothing. When $R \gg \Gamma$ f approaches its maximum value, which depends on the relative probe and coupling beam diameters. Experimentally, the changes in f can be calculated for different ratios R/Γ by taking the ratio of the values for $R+\Gamma$ in Figs. 15 and 16 and the measured EIT FWHM from Fig. 9. For coupling powers of $P_c=0.34$ mW, $P_c=1$ mW, and $P_c=1.9$ mW we find that $f \approx 1$, $f \approx 1.3$, and $f \approx 1.4$, respectively. This agrees with the fact that as the optical pumping rate increases the diffusion length decreases and the value of f monotonically approaches its maximum value. The maximum value of $f \approx 1.5$ can be calculated by spatial averaging while assuming an infinitesimal diffusion length.

VI. CONCLUSIONS

The transients and rise times of the EIT Kerr nonlinearity are well modeled by the theory of Ref. [21] (this theory is also reviewed in Sec. II). This agreement between theory and experiment is especially good for the refractive Kerr nonlinearity when intensity variations in the fields (e.g., Gaussian beam shapes) are accounted for. Also, by thinking in terms of the GSC it is possible to develop a more intuitive understanding of the physical mechanisms behind the EIT Kerr nonlinearity and its dynamics.

Our primary result is that the rise and fall times of the refractive Kerr nonlinearity are accurately predicted by Eq. (13) for the small Raman detunings. This means that in the limit of greatest interest for most EIT Kerr applications (i.e., $\alpha L \gg 1$ and $\delta_R \ll R$), the EIT Kerr rise time is inversely proportional to the optical thickness and linearly proportional to the EIT linewidth.

Both of these proportionalities may prove problematic for pulsed applications of the refractive EIT Kerr nonlinearity such as QND measurements of photon number. Pulsed EIT Kerr applications require a strong nonlinear response at low pulse energies, which implies that the EIT Kerr nonlinearity should be both large and fast. However, one advantage of the EIT Kerr nonlinearity is that it can theoretically be made arbitrarily large because it is linearly proportional to the optical thickness and inversely proportional to the EIT linewidth. Thus, making the EIT Kerr nonlinearity large also makes it slow and vice versa. Applications that are limited by the slow rise time of the EIT Kerr nonlinearity include: QND measurement of photon number, entangling optical wave packets, synthesis of number states, and single photon sources and detectors. All of these applications require pulsed few-photon operation.

Although the slow rise time of EIT Kerr nonlinearity limits its applicability, the EIT Kerr nonlinearity is still comparatively large relative to other Kerr nonlinearities, and it has other advantages such as weak self-phase modulation. In most parametric nonlinear processes the rise time is so fast that it is ignored. For EIT enhanced nonlinear processes the rise time is sufficiently slow that it cannot be ignored for most applications.

ACKNOWLEDGMENTS

This work was supported by DARPA Slow Light, the National Science Foundation, and Research Corporation.

APPENDIX: CALCULATIONS OF AVERAGE OPTICAL PUMPING RATE AND EFFECTIVE HOMOGENEOUS LINEWIDTH

In this appendix we discuss how the complicated ^{85}Rb system can be distilled into a couple of parameters: The average optical pumping rate R_{ave}, and the effective homogeneous linewidth γ_{eff}. These parameters allow us to use the simple four-level theory of Sec. II to predict the EIT dynamics in ^{85}Rb. In the experiment EIT is created on the D_1 line of ^{85}Rb using orthogonal linearly polarized probe and coupling beams. Choosing the quantization axis along coupling beam polarization, Fig. 19 shows the probe and coupling transitions with their transition coefficients.

In order to achieve coherent population trapping and EIT, the dark states must be simultaneously dark for both the $F'=2$ and $F'=3$ excited hyperfine levels. There is only one superposition of ground states that satisfies this condition.

There are also four other semidark states which are not completely decoupled from the excited states, but are more weakly coupled to the excited than the bright states. To calculate the coupling between the ground and excited states we solve for the eigenvalues of the time independent Hamiltonian. The Hamiltonian accounts for only the D_1 line dipole allowed transitions explicitly shown in Fig. 19 and includes all field and detuning parameters while assuming a rotating reference frame and the rotating wave approximation. The eigenvalues and eigenvectors are calculated for the case when $\delta_R=0$ and $\Delta \gg \Omega_+$, where

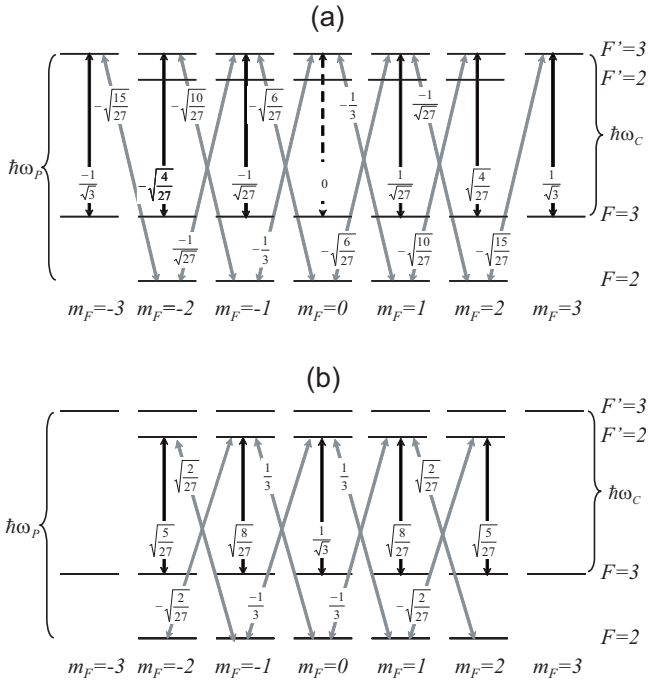

FIG. 19. (Color online) Transitions excited by the vertically polarized probe laser (gray lines) and horizontally polarized coupling laser (black lines). The quantization axis is chosen along the horizontal polarization. Also shown are the hyperfine matrix elements for each excited transition, which are related to the Clebsch-Gordon coefficients by the factor $(-1)^{F'+J+1+I}\sqrt{(2F'+1)(2J+1)}\left\{\begin{matrix} J & J' & 1 \\ F' & F & I \end{matrix}\right\}$, where $I=3/2$ is the nuclear spin, $J=J'=1/2$ are the orbital plus spin angular momenta for the ground and excited state, respectively, and we have used the Wigner 6-j symbol.

$$\Omega_+ = 2\mu_{D_1}\sqrt{E_P^2 + E_C^2}/\hbar\sqrt{3}, \tag{A1}$$

is the back-of-the-envelope "bright" Rabi frequency for the D_1 line and where $\mu_{D_1}=2.54\times10^{-29}$ C m is the dipole moment for the D_1 line ($\mu_{D_1}\approx\mu_{D_2}/\sqrt{2}$). The calculated eigenvalues are the Stark shifted excited and ground state energies, and the amount of the Stark shift gives the strength of the coupling. The 12 eigenvectors with eigenvalues closest to the original ground state energy can be projected onto the ground states and normalized to create a new orthonormal basis for the ground states. The Stark shifts of the energy for these new basis ground states are used to determine the Rabi frequency Ω_i using

$$\Delta U_i = -\Omega_i^2/4\Delta, \quad i=\{1,2,\ldots,12\}, \tag{A2}$$

where ΔU_i is the Stark shift for each of the ground states. Figure 20 shows each of the 12 ground state Rabi frequencies Ω_i normalized by the back-of-the-envelope "bright" Rabi frequency Ω_+ plotted as a function of the ratio between probe and coupling field amplitudes E_P/E_C (for the experiment discussed in this paper $0.2\geq\Omega_P/\Omega_C\leq0.6$). A new orthonormal basis for the excited states can be calculated by projecting the 12 excited state eigenvectors onto the excited states and normalizing. Each of the new basis ground states will couple to one of the new basis excited states with the exception of the completely dark states which are completely decoupled from all other states.

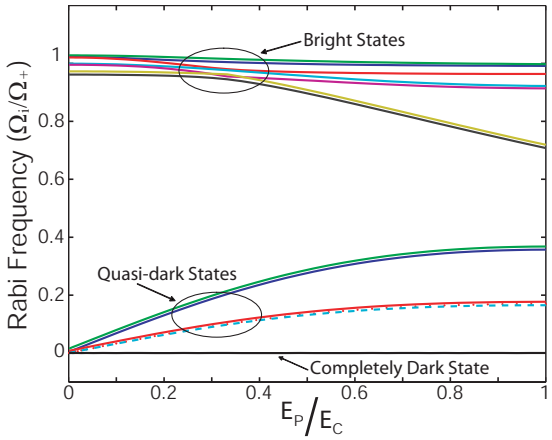

FIG. 20. (Color online) Normalized Rabi frequencies Ω_i/Ω_+ plotted versus the ratio E_P/E_C. There are 12 Rabi frequencies: seven bright states, four quasidark states, and one completely dark state.

The effective optical pumping rate can be approximated as the average of the optical pumping rates out of each bright state into one of the five dark states. The optical pumping rate out of bright state m is given by

$$R_m = \sum_{n=1}^{5}\sum_{l=1}^{12} P(e_l|+_m)R_{|e\rangle_l\rightarrow|-\rangle_n}, \tag{A3}$$

where $P(e_l|+_m)$ is the steady-state conditional probability that if the atom is in either bright state $|+\rangle_m$ or one of the excited states, then it is in excited state $|e\rangle_l$, and $R_{|e\rangle_l\rightarrow|-\rangle_n}$ is the spontaneous decay rate from excited state $|e\rangle_l$ to dark state $|-\rangle_n$. The effective optical pumping rate is then

$$R_{\text{ave}} = \frac{1}{7}\sum_{m=1}^{7} R_m, \tag{A4}$$

where we have assumed that the bright states are equally populated in steady state (in reality there will be some varia-

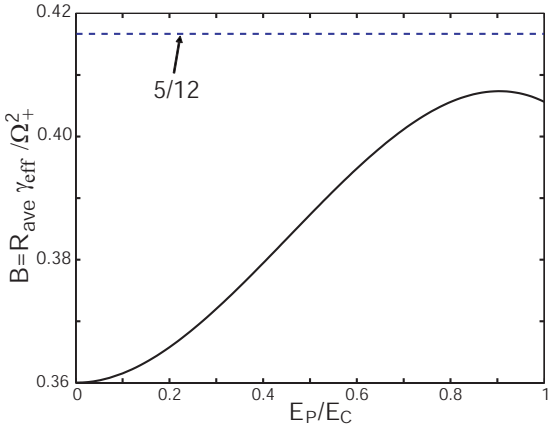

FIG. 21. (Color online) Plot of $B=R_{\text{ave}}\gamma_{\text{eff}}/\Omega_+^2$ versus the ratio E_P/E_C. Also plot is the value 5/12=0.417, which is the ratio of the number of dark states to ground states. Over the range $0.2\geq E_P/E_C\leq0.6$ B is approximately 3/8.

tion in the bright state populations but it should be small for the parameters considered in the experiment). Evaluating Eq. (A4) we find that in the range $0.2\Omega_C \leq \Omega_p \geq 0.6\Omega_C$ that

$$R_{\text{ave}} \approx \frac{3\Omega_+^2}{8\gamma_{\text{eff}}}, \tag{A5}$$

where γ_{eff} is the effective homogeneous linewidth that arises due to a combination of Doppler broadening and buffer gas effects. Figure 21 shows the value of $R_{\text{ave}}\gamma_{\text{eff}}/\Omega_+^2$ as a function of Ω_P/Ω_C. Naively one might expect this value to be 5/12, which is the ratio between the number of bright states and the total number of ground states, but calculations shown in 21 reveal that it is slightly smaller than 5/12 and is weakly dependent on the ratio Ω_P/Ω_C.

The optical pumping rate also has a spatial dependence due to the inhomogeneity of the field intensities (i.e., the beams are approximately Gaussian). Thus quantities that are dependent on the optical pumping rate such as the rise times and transparency FWHM must be averaged spatially.

There are two primary contributions to the effective homogeneous linewidth: homogeneous broadening due to the buffer gas and Doppler broadening. The buffer gas actual has two distinct effects. First, collisions between ^{85}Rb and N_2 atoms change the velocities of the atoms. Second, the collisions randomize the phase of the $5S_{1/2} \rightarrow 5P_{1/2}$ transitions which broadens the homogeneous linewidth. For ^{85}Rb with a N_2 buffer gas the measured increase in homogeneous linewidth is 16.3 MHz per Torr N_2 [36,37]. In our experiment we have 20 Torr N_2 resulting in $\gamma_\perp = 330$ MHz before considering Doppler broadening. Although buffer gas collisions randomize the phase of the $5S_{1/2} \rightarrow 5P_{1/2}$ coherences, the ground state coherences (GSC) are essentially unaffected by the ^{85}Rb-N_2 collisions. Because the ^{85}Rb-N_2 collision rate, which is about $2\pi \times 50$ MHz, is much faster than the optical pumping rate in the experiment $R \sim 30$ kHz, the atoms will on average "wander" through every velocity class several times in one optical pumping period $T = 1/R$ without loss of ground state coherence (GSC). Thus, processes such as EIT which are determined by the GSC must be averaged over the contributions from all velocity classes. Thus the effective homogeneous linewidth is

$$\frac{1}{\gamma_{\text{eff}}} = \frac{\gamma_\perp}{\sqrt{2\pi}\Delta_D} \int_{-\infty}^{\infty} \frac{\exp\left(-\frac{\Delta^2}{2\Delta_D^2}\right)}{4\Delta^2 + \gamma_\perp^2} d\Delta, \tag{A6}$$

and $\gamma_{\text{eff}} = 660$ MHz when $\Delta_D = 530$ MHz and $\gamma_\perp = 330$ MHz.

[1] P. R. Hemmer, D. P. Katz, J. Donoghue, M. Cronin-Golomb, M. S. Shahriar, and P. Kumar, Opt. Lett. **20**, 982 (1995).
[2] H. Schmidt and A. Imamoglu, Opt. Lett. **21**, 1936 (1996).
[3] S. E. Harris and Y. Yamamoto, Phys. Rev. Lett. **81**, 3611 (1998).
[4] S. E. Harris and L. V. Hau, Phys. Rev. Lett. **82**, 4611 (1999).
[5] G. M. D'Ariano, L. Maccone, M. G. A. Paris, and M. F. Sacchi, Phys. Rev. A **61**, 053817 (2000).
[6] M. Fleischhauer and M. D. Lukin, Phys. Rev. Lett. **84**, 5094 (2000).
[7] M. D. Lukin and A. Imamoglu, Phys. Rev. Lett. **84**, 1419 (2000).
[8] M. Yan, E. G. Rickey, and Y. Zhu, Phys. Rev. A **64**, 041801(R) (2001).
[9] E. Paspalakis and P. L. Knight, J. Mod. Opt. **49**, 87 (2002).
[10] D. Petrosyan and G. Kurizki, Phys. Rev. A **65**, 033833 (2002).
[11] H. Kang and Y. Zhu, Phys. Rev. Lett. **91**, 093601 (2003).
[12] D. A. Braje, V. Balic, G. Y. Yin, and S. E. Harris, Phys. Rev. A **68**, 041801(R) (2003).
[13] A. B. Matsko, I. Novikova, G. R. Welch, and M. S. Zubairy, Opt. Lett. **28**, 96 (2003).
[14] D. A. Braje, V. Balić, S. Goda, G. Y. Yin, and S. E. Harris, Phys. Rev. Lett. **93**, 183601 (2004).
[15] R. G. Beausoleil, W. J. Munro, and T. P. Spiller, J. Mod. Opt. **51**, 1559 (2004).
[16] Y.-F. Chen, G.-C. Pan, and I. A. Yu, Phys. Rev. A **69**, 063801 (2004).
[17] M. Fleischhauer, A. Imamoglu, and J. P. Marangos, Rev. Mod. Phys. **77**, 633 (2005).
[18] V. Balić, D. A. Braje, P. Kolchin, G. Y. Yin, and S. E. Harris, Phys. Rev. Lett. **94**, 183601 (2005).
[19] C. Ottaviani, S. Rebic, D. Vitali, and P. Tombesi, Phys. Rev. A **73**, 010301(R) (2006).
[20] E. Knill, R. Laflamme, and G. Milburn, Nature (London) **409**, 46 (2001).
[21] M. V. Pack, R. M. Camacho, and J. C. Howell, Phys. Rev. A **74**, 013812 (2006).
[22] H. Wang, D. Goorskey, and M. Xiao, Opt. Lett. **27**, 1354 (2002).
[23] Y.-F. Chen, G.-C. Pan, and I. A. Yu, J. Opt. Soc. Am. B **21**, 1647 (2004).
[24] S. J. Park, H. Cho, T. Y. Kwon, and H. S. Lee, Phys. Rev. A **69**, 023806 (2004).
[25] A. Godone, S. Micalizio, and F. Levi, Phys. Rev. A **66**, 063807 (2002).
[26] K. Harada, K. Motomura, T. Koshimizu, H. Ueno, and M. Mitsunaga, J. Opt. Soc. Am. B **22**, 1105 (2005).
[27] A. Mair, J. Hager, D. F. Phillips, R. L. Walsworth, and M. D. Lukin, Phys. Rev. A **65**, 031802(R) (2002).
[28] P. Valente, H. Failache, and A. Lezama, Phys. Rev. A **65**, 023814 (2001).
[29] A. Belyanin, C. Bentley, F. Capasso, O. Kocharovskaya, and M. O. Scully, Phys. Rev. A **64**, 013814 (2001).
[30] M. Lindberg and R. Binder, Phys. Rev. Lett. **75**, 1403 (1995).
[31] Y. Wu and X. Yang, Phys. Rev. A **71**, 053806 (2005).
[32] D. Budker, D. F. Kimball, S. M. Rochester, and V. V. Yashchuk, Phys. Rev. Lett. **83**, 1767 (1999).
[33] L. Hau, S. Harris, Z. Dutton, and C. Behroozi, Nature (London) **397**, 594 (1999).
[34] R. S. Bennink, Ph.D. thesis, University of Rochester, Institute of Optics, 2004.

[35] Transit-time broadening derives from atomic diffusion resulting in optically prepared atoms in the laser beam being replaced by thermal atoms from outside the beam.
[36] J. Vanier and A. Audoin, *The Quantum Physics of Atomic Frequency Standards* (Adam Hilger, Philadelphia, 1989).
[37] M. D. Rotondaro and G. P. Perram, J. Quant. Spectrosc. Radiat. Transf. **57**, 497 (1997).